ADVANCED FUNCTIONAL MATERIALS
www.afm-journal.de

Enhancing Temperature Responsiveness of PNIPAM Through 3D-Printed Hierarchical Porosity

Weiyi Liu, Zhenwu Wang, Julian A. Serna, Rafaela Debastiani, Joaquin E. Urrutia Gomez, Lutong Lu, Wenwu Yang, Zheqin Dong, and Pavel A. Levkin**

Materials with ultra-fast responsive properties are essential for various applications. Among the responsive materials, poly(*N*-isopropylacrylamide) (PNIPAM) stands out due to its well-studied temperature-responsive properties. Improving the kinetics of the responsive properties of PNIPAM is, however, still essential for advancing its practical use. Here, the responsive rate of PNIPAM hydrogels is enhanced by first incorporating sub-micrometer porosity into the material through polymerization-induced phase separation (PIPS), followed by introducing millimeter scale pores via 3D printing, thereby rendering the material with hierarchical porosity. The 3D-printed porous PNIPAM structures show accelerated swelling and deswelling, when compared to non-porous PNIPAM structures, due to enhanced water permeability associated with the continuous network of micrometer to millimeter-sized pores. Additionally, thinner polymer structures result in faster temperature response rates. At the same time, the mechanical strength of PNIPAM hydrogels with high porosity and thinner polymer walls is not compromised, overcoming the common trade-off between swelling and mechanical properties.

1. Introduction

Materials, which properties can change in response to external stimuli (e.g., light, temperature, pH, strain, stress, magnetic, acoustic, electric, etc.), are indispensable across various applications such as soft robotics, aerospace engineering, flexible electronics, and tissue engineering.[1–5] One promising and well-characterized temperature-responsive material is poly(*N*-isopropylacrylamide) (PNIPAM),[6–9] which is hydrophilic at room temperature and exhibits a lower critical solution temperature (LCST) at ≈32 °C.[10] The proximity of LCST of PNIPAM to body temperature renders it highly appealing for biomedical applications.[11] While PNIPAM exhibits swift response speeds at the molecular scale,[12–14] its apparent responsiveness at larger, millimeter to centimeter-scale, is slow.[15–17] This limitation mainly stems from the constraints imposed by the slow stimuli transmission speed as well as the slow speed of water expelling from the bulk hydrated PNIPAM.[18–19] Several strategies have been proposed to accelerate the response rate of PNIPAM hydrogels. One approach is based on reducing the hydrogel structure size, as the responsive rate of hydrogels is inversely proportional to the square of the material´s smallest dimension.[20] However, it is obviously not applicable to large structures. An alternative

W. Liu, Z. Wang, J. A. Serna, J. E. U. Gomez, Z. Dong, P. A. Levkin
Institute of Biological and Chemical Systems-Functional Molecular Systems (IBCS-FMS)
Karlsruhe Institute of Technology (KIT)
Hermann-von Helmholtz-Platz 1, 76344 Eggenstein-Leopoldshafen, Germany
E-mail: zheqindong@sdu.edu.cn; pavel.levkin@kit.edu

W. Liu
College of Environment Sciences
Sichuan Agricultural University
Huimin Road 211, 611130 Chengdu, China

The ORCID identification number(s) for the author(s) of this article can be found under https://doi.org/10.1002/adfm.202403794

DOI: 10.1002/adfm.202403794

R. Debastiani, W. Yang
Institute of Nanotechnology (INT)
Karlsruhe Institute of Technology (KIT)
Kaiserstr. 12, 76131 Karlsruhe, Germany

R. Debastiani
Karlsruhe Nano Micro Facility (KNMFi)
Karlsruhe Institute of Technology (KIT)
Hermann-von-Helmholtz-Platz 1, 76344 Eggenstein-Leopoldshafen, Germany

L. Lu
Institute for Micro Process Engineering (IMVT)
Karlsruhe Institute of Technology (KIT)
Hermann-von-Helmholtz-Platz 1, 76344 Eggenstein-Leopoldshafen, Germany

Z. Dong
School and Hospital of Stomatology
Cheeloo College of Medicine Shandong University & Shandong Key Laboratory of Oral Tissue Regeneration & Shandong Engineering Laboratory for Dental Materials and Oral Tissue Regeneration
No. 44-1 Wenhuaxi Road, Jinan, Shandong 250012, China

approach involves the introduction of porosity into PNIPAM, which promotes the responsive rate by facilitating water expulsion.[21–23] He and colleagues recently reported porous PNIPAM created via cononsolvency photo-polymerization, thus boosting the response rate of the material.[24] Drawing inspiration from the existing strategies, hierarchical interconnected porosity with pores spanning from nano- to millimeter hold significant promise for further enhancing the response speed of macroscopic PNIPAM structures.

Polymerization-induced phase separation (PIPS) is a method to produce meso- to macroporous polymers, providing access to materials with controlled porosity at various scales. In this process, the miscibility of the growing polymer chains in the solvent differs from that of the monomers, which results in a polymer-rich phase that forms the porous matrix and a polymer-poor phase that provides porosity.[25–27] Such technology has been already applied for chromatography, microfluidics, membranes, and drug delivery, confirming its feasibility in the construction and control of porous polymer structures.[28–30] 3D printing enables highly customized 3D shaping of materials from micro- to millimeters and above.[31–32] Recently, polymerization-induced phase separation was combined with 3D printing to create hierarchical porous 3D structures.[25,33]

In this work, we employ a two-fold approach to increase the responsiveness of macroscopic PNIPAM hydrogel structures. Initially, sub-micrometer porosity was incorporated into the PNIPAM using PIPS. Subsequently, millimeter-scale pores were introduced via 3D printing, thereby endowing the material with a hierarchically porous structure. First, we investigated the solvent effect on the microporous structures formed during PIPS, achieving high porosity, low porosity, and non-porosity of PNIPAM using ethylene glycol (EG), water, and dimethylformamide (DMF), respectively. High porosity correlated with thin polymer walls, whereas low porosity correlated with thicker polymer walls. We then conducted a comprehensive characterization of the pores created by different solvents and established the relationship between water diffusion and the resulting porous structures. Moreover, the tunable macro-porous structures created by 3D printing were used to further enhance the response rate and realize the anisotropic actuation. Based on the designed hierarchically porous structures, the PNIPAM showed a 45.5% volume change in 10 seconds. We believe that this hierarchical structuring strategy, which combines 3D printing with PIPS, can be readily applied to other smart materials to enhance their responsiveness. Such enhancement is crucial for advancing their application in fields where ultra-fast responsiveness is required such as sensors, actuators, and energy harvesting.

2. Results and Discussion

To fabricate 3D PNIPAM structures using digital light processing (DLP) 3D printing, we used *N*-isopropylacrylamide (NIPAM) mixed with one of three porogenic agents: EG, water, or DMF. Among them, water and DMF were more miscible with the NIPAM monomer than EG. Once the printed gel structures were post-processed by incubating them in water to exchange the porogens with water, three different porous configurations were obtained (**Figure 1**). As evidenced from scanning electron microscopy (SEM), PNIPAM-EG structures showed thin polymer walls while PNIPAM-Water structures showed thick polymer walls (**Figure 2**d,f). In contrast, 3D printing NIPAM in DMF resulted in non-porous PNIPAM-DMF structures. Hence, the presence and configuration of porosity (high, low, or no) could be tuned via the selection of porogens. PIPS during 3D printing in EG and water resulted in the formation of PNIPAM-rich phases and PNIPAM-poor phases due to the weak miscibility of EG and water.[33] While all PNIPAM hydrogels exhibited deswelling at 40 °C followed by swelling at 25 °C (**Figure 3**b), PNIPAM-EG hydrogel displayed a much faster thermo-responsive rate than PNIPAM-Water and PNIPAM-DMF hydrogels (Figure 3a,b), presumably resulting from the high porosity and thin polymer walls induced by phase separation (Figure 2e,h).

PNIPAM-DMF hydrogel was semi-transparent (Figure 2a) with an average transmittance of ≈37% between 400 and 800 nm (Figure 2b) as measured by UV/Vis spectrometry. In contrast, both PNIPAM-Water and PNIPAM-EG hydrogels appeared opaque with an average transmittance of ≈5%, indicating strong light scattering caused by pores. The water content after solvent exchange was ≈72% for PNIPAM-Water hydrogel, slightly lower than that of PNIPAM-EG and PNIPAM-DMF hydrogels (above 80%) (Figure 2c). Such difference suggested the denser polymer network in the PNIPAM-Water hydrogel. Comparatively, the transmittance and solvent fraction of as-printed PNIPAM gels are shown in Figure S1 (Supporting Information).

Importantly, SEM imaging and X-ray nano-computed tomography (nano-CT) characterization,[34] revealed distinct microstructures for the three types of PNIPAM hydrogels. SEM images of the cross-section showed that the boundary between the printing layers was lightly visible in PNIPAM-Water hydrogel (Figure 2d), was clear and distinct in PNIPAM-EG hydrogel (Figure 2e) but was not visible in PNIPAM-DMF hydrogels (Figure 2f), respectively. Compared with homogeneous-porous PNIPAM-Water hydrogel, PNIPAM-EG hydrogel was gradient-porous in each printing layer, likely attributed to the reduced light intensity within each layer during 3D printing. Specifically, regions of the PNIPAM-EG layer farther from the light source experienced lower UV intensity, resulting in dense pores. The presence of pores proved that PIPS occurred when using either water or EG as a solvent. Conversely, PNIPAM-DMF hydrogel appeared non-porous, meaning that PIPS did not occur when employing DMF. This was due to the lower miscibility of the NIPAM monomer in EG and water than in DMF. Clearly, porogenic agent plays a crucial role in controlling the microstructure of the hydrogels. In addition, the surfaces of three PNIPAM hydrogels were shown in Figure S2 (Supporting Information), indicating that strong PIPS occurred on PNIPAM-EG.

Moreover, the absence of pores (larger than 128 nm, a pixel size of nano-CT) in PNIPAM-DMF hydrogel was identified with nano-CT, while the interconnected pores of both PNIPAM-Water and PNIPAM-EG were confirmed (Figure 2g–i; Figure S3 and Movie S1, Supporting Information). Furthermore, quantitative results (Table S1, Supporting Information) revealed a significant disparity in porosity (volume of pores/total volume) between the sparse- and dense-pore regions of PNIPAM-EG (6.4%), compared to the porosity difference between two selected regions of PNIPAM-Water (0.86%). This indicated the presence of high porosity in PNIPAM-EG and low porosity in PNIPAM-Water. Meanwhile, the surface area of PNIPAM-EG (5.62 μm^{-1}) was

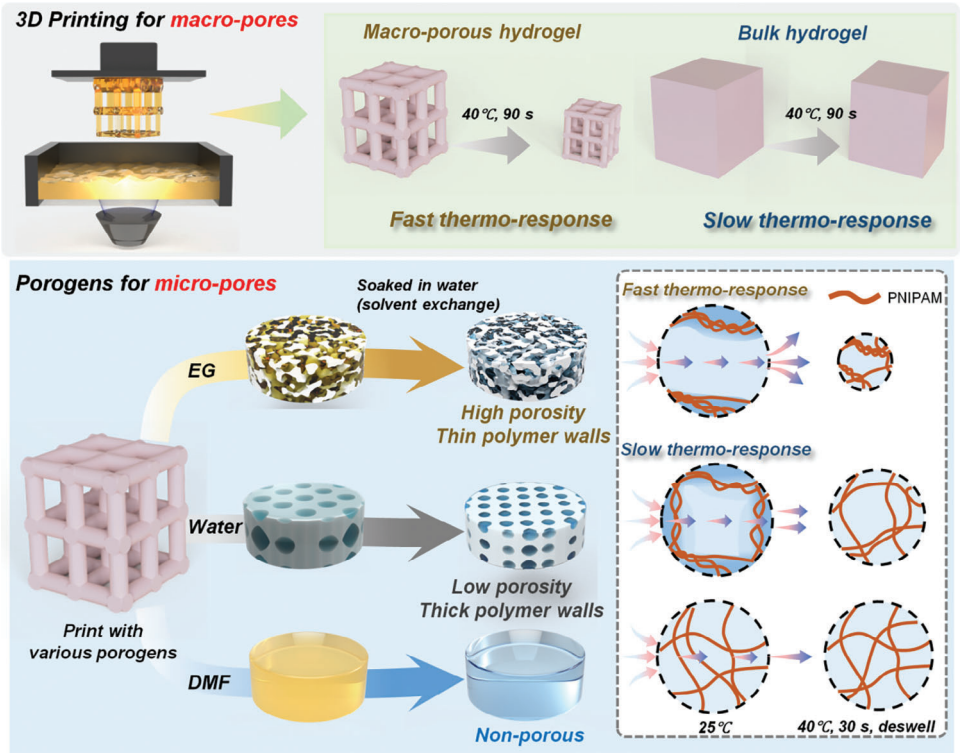

Figure 1. Schematic showing DLP 3D-printed PNIPAM hydrogels with high porosity, low porosity, and non-porosity by using EG, water, and DMF, respectively, which leads to distinct thermo-responsive kinetics.

significantly higher than that of PNIPAM-Water (3.73 μm^{-1}), indicating the thin polymer wall of PNIPAM-EG polymers and the thick polymer wall of PNIPAM-Water (Figure S4 and Table S1, Supporting Information). PNIPAM has a solubility parameter of 11.5 $cal^{1/2}$ $cm^{-3/2}$, while DMF, EG, and Water have solubility parameters of 12.1, 16.3, and 23.5 $cal^{1/2}$ $cm^{-3/2}$, respectively.[35–36] Consistent with these solubility parameters, in experiments we found that the NIPAM monomer rapidly dissolved in DMF but dissolved much more slowly in water and EG, indicating superior miscibility of PNIPAM with DMF. This discrepancy explains why PIPS occurs in EG and water but not in DMF, resulting in porous PNIPAM-EG and PNIPAM-Water hydrogels, while PNIPAM-DMF hydrogels remain non-porous. Furthermore, solubility parameters indicate that water is a poorer solvent than EG, which may lead to an earlier stage of PIPS and the formation of a coarser polymer phase.[33] Indeed, SEM and nano-CT analyses reveal that PNIPAM-Water hydrogels have thicker polymer walls and lower porosity compared to PNIPAM-EG. Overall, the miscibility of porogens with PNIPAM influences the extent of PIPS and, consequently, the porosity of the hydrogels. It is important to note that the samples analyzed with SEM and nano-CT were prepared by freeze-drying, which might have led to a deviation from the original wet structure. Finally, Fourier-transform infrared spectroscopy (FTIR) measurements on freeze-dried samples did not reveal noticeable differences between all three samples, suggesting their identical chemical structure (Figure S5, Supporting Information).

To investigate the influence of microstructure on the thermo-responsive performance of PNIPAM hydrogels, we conducted deswelling and swelling tests by immersing the hydrogel into a water bath at 40 °C and then transferring it into one at 25 °C, while monitoring changes in volume. Since the LCST of PNIPAM is ≈32 °C,[37] all PNIPAM hydrogels shrank at 40 °C and swelled back upon being exposed to water at 25 °C (Figure 3a,b; Movie S2, Supporting Information). Meanwhile, PNIPAM hydrogels shrank at 50 and 60 °C, showing the same tendency (Figure S6, Supporting Information). Among the three hydrogels, PNIPAM-EG hydrogel demonstrated the fastest deswelling and swelling rate, which can be attributed to its high porosity and thin polymer walls facilitating water transport in and out upon swelling and deswelling, respectively. Interestingly, although PNIPAM-Water hydrogel showed a higher deswelling rate than PNIPAM-DMF, it had a slower swelling rate (Figure 3a,b). During the deswelling process, the porous structure of PNIPAM-Water was favorable for water diffusion, in contrast to the non-porous structure of PNIPAM-DMF. However, during the swelling process, the porous structure of PNIPAM-Water hydrogel collapsed in the shrunken state (Figure S7, Supporting Information). Consequently, its thick polymer walls impeded both water diffusion and swelling rate.

To explore the influence of microstructure on both c of PNIPAM hydrogels and diffusion rate through the pores, we compared the kinetics of both dye infiltration and dye diffusion out of three different hydrogels. PNIPAM hydrogels preincubated at 25 °C were immersed in a 0.01 wt% Rhodamine B (RhB) aqueous solution. The samples were retrieved at various time points until equilibrium was achieved, and the dye penetration depth was subsequently analyzed (Figure 3c,d). Subsequently, additional

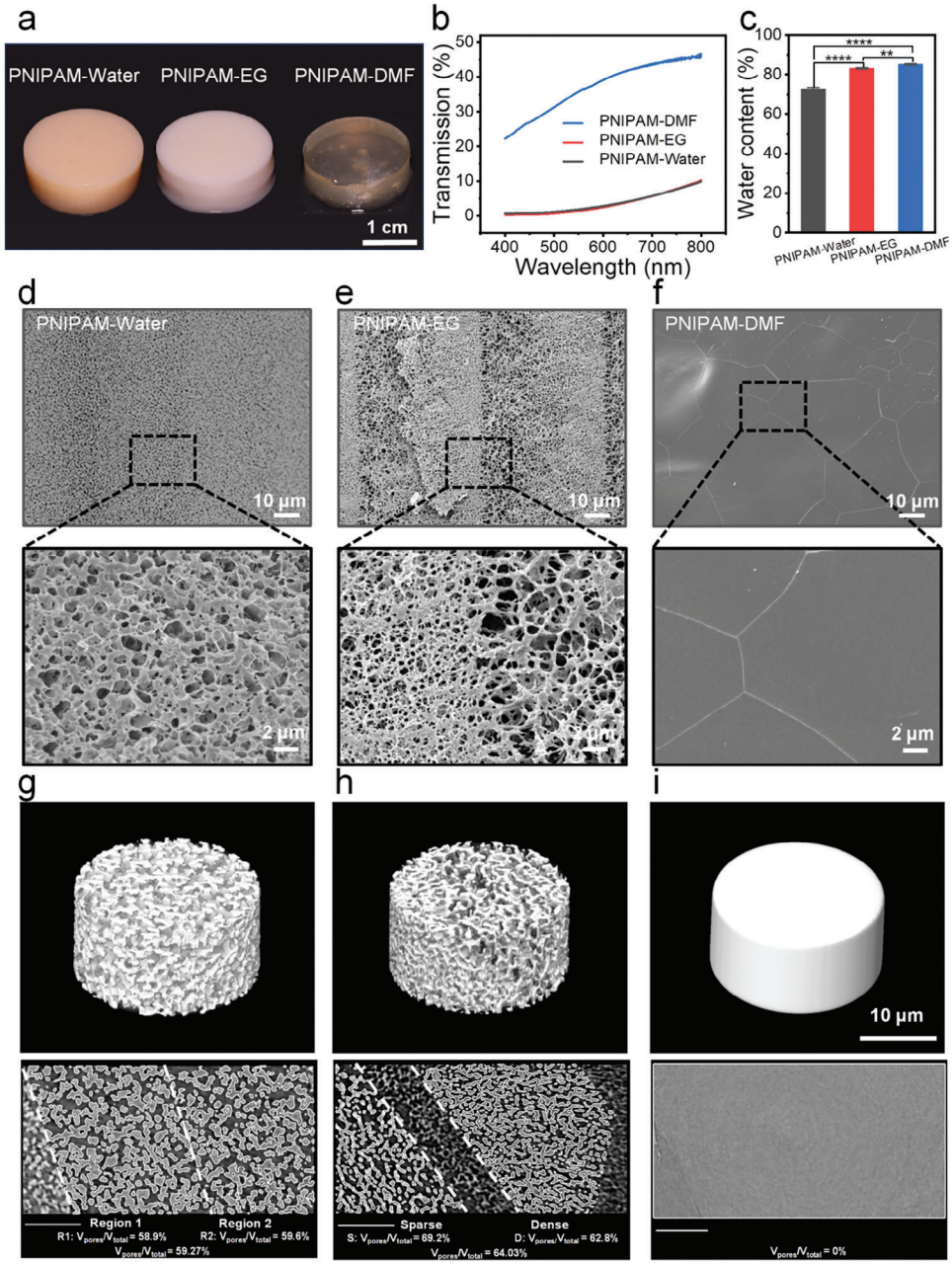

Figure 2. Characterization of PNIPAM-Water, -EG, and -DMF hydrogels. a) Photos of the hydrogel cylinders after exchange of solvents with water. b) Light transmittance through PNIPAM hydrogels (sample thickness: 500 μm). c) The water content of PNIPAM hydrogels (wt%). d–f) SEM showing the cross-section of PNIPAM hydrogels and g–i) NanoCT 3D reconstructed volume and segmented plots of PNIPAM hydrogels.

samples were immersed in pure water (25 °C) and their cross-sections were analyzed for the dye release (Figure 3c). The findings indicated that the sequence of diffusion rates for both dye absorption and release processes was as follows: PNIPAM-EG > PNIPAM-DMF > PNIPAM-Water. This confirmed our hypothesis that high porosity and thin polymer walls of PNIPAM-EG hydrogel significantly enhanced the water diffusion kinetics, resulting in a rapid deswelling and swelling rate. Conversely, PNIPAM-Water hydrogel exhibited the slowest dye diffusion kinetics, which corresponded to its slow swelling rate at 25 °C.

The mechanical properties of PNIPAM hydrogels played a crucial role in their application. Consequently, we performed mechanical tests on PNIPAM hydrogels under both swollen (25 °C) and shrunken states (40 °C). The results showed a trend where all PNIPAM hydrogels displayed higher strength in the shrunken state as compared to the swollen state, which can be primarily attributed to the dense polymer matrix (Figure 3e,f). A two-way ANOVA test revealed that both the solvent (water, EG, or DMF) and the state of the polymer wall (swollen or shrunken) had a significant effect on the Young's modulus of the hydrogels

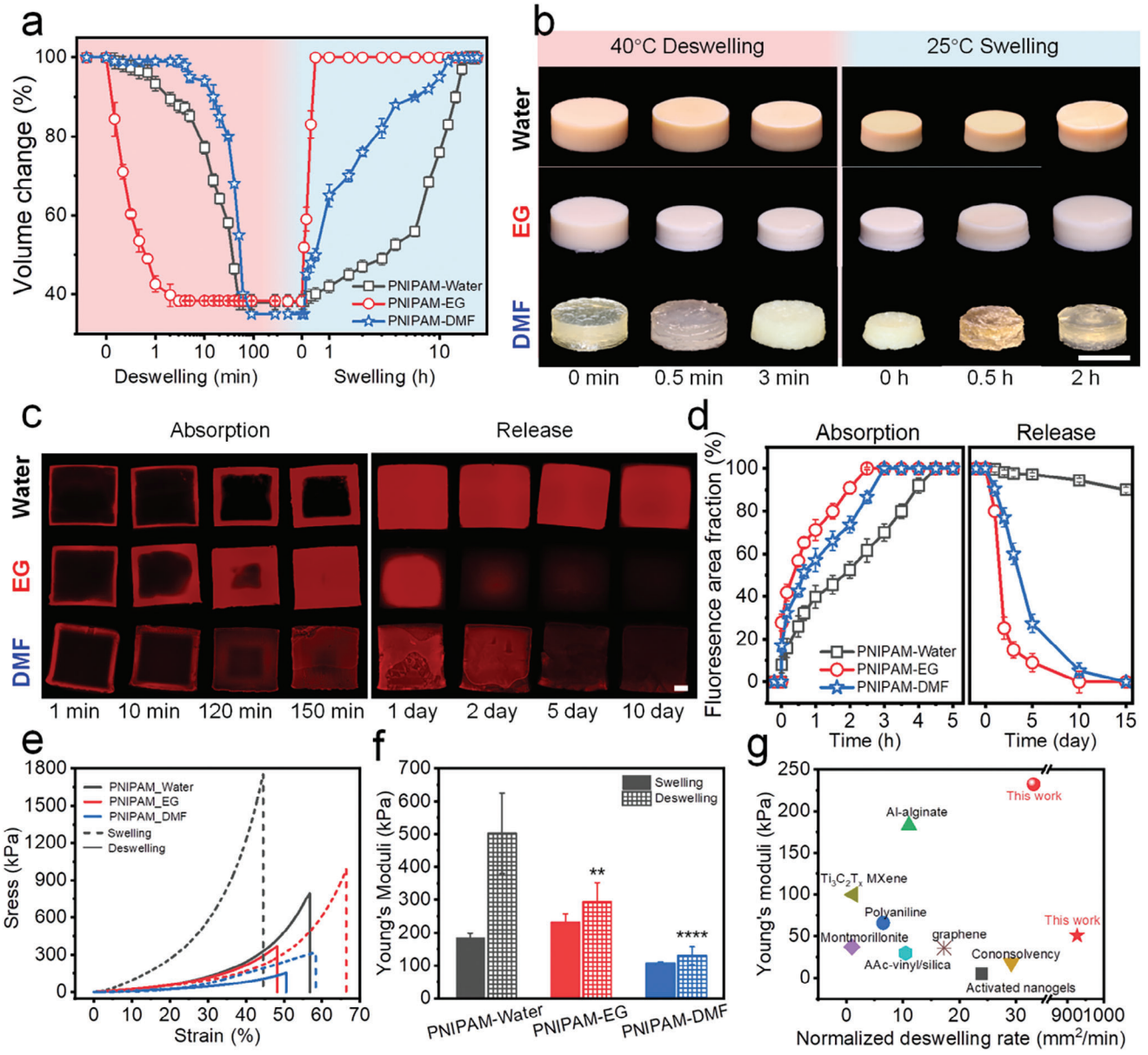

Figure 3. Thermo-responsive and mechanical properties of 3D-printed PNIPAM hydrogels produced using Water, EG, and DMF as porogens. a) Deswelling (40 °C) and swelling (25 °C) curves and b) digital photos for PNIPAM hydrogels, respectively (Scale bar: 1 cm). c) Fluorescence microscopy images showing the diffusion kinetics of RhB dye into and out of PNIPAM hydrogels at 25 °C (Scale bar: 1 mm). (d) The ratio of fluorescent area to the total area for PNIPAM hydrogels during the dye absorption and release process. e) Stress–strain curves and f) Young's modulus of the swollen and shrank PNIPAM hydrogels. (*) in the bars for shrunk PNIPAM-EG and PNIPAM-DMF denote their level of statistically significant difference with PNIPAM-Water hydrogels in the same state. g) Comparison of Young's modulus and normalized deswelling rate with the previous works (the red ball was a bulk cylinder and the red star was a cobweb cylinder). The compared works included PNIPAM prepared with activated nanogels,Ref. [15] polyaniline, Ref. [22] Al-alginate, Ref. [24] montmorillonite, Ref. [36] cononsolvency, Ref. [38] AAc-vinyl/silica, Ref. [39] graphene Ref. [40] and $Ti_3C_2T_x$ MXene. Ref. [41]

($p < 0.0001$ and $p < 0.001$, respectively). Notably, among the swollen hydrogels, PNIPAM-DMF exhibited the lowest Young's modulus and strength, likely stemming from its comparatively lower material density (Figure 2c). Surprisingly, even though PNIPAM-EG hydrogel possessed higher water content, its Young's modulus was twice as high as that of PNIPAM-Water hydrogel. This was attributed to the synergistic effect and good integration of sparse and dense regions of PNIPAM-EG.[21,38–39] Notably, the contracted state of PNIPAM-Water exhibited Young's modulus of 500 kPa, significantly higher than that of the EG and DMF counterparts ($p < 0.01$ and $p < 0.0001$, respectively), indicating its dense polymer matrix, which might explain its slower swelling rate (Figure 3d). It is important to mention that 3D-printed objects generally exhibited mechanical anisotropy due to the layer-by-layer construction process. Indeed, Young's modulus of PNIPAM-EG in the parallel direction of printing

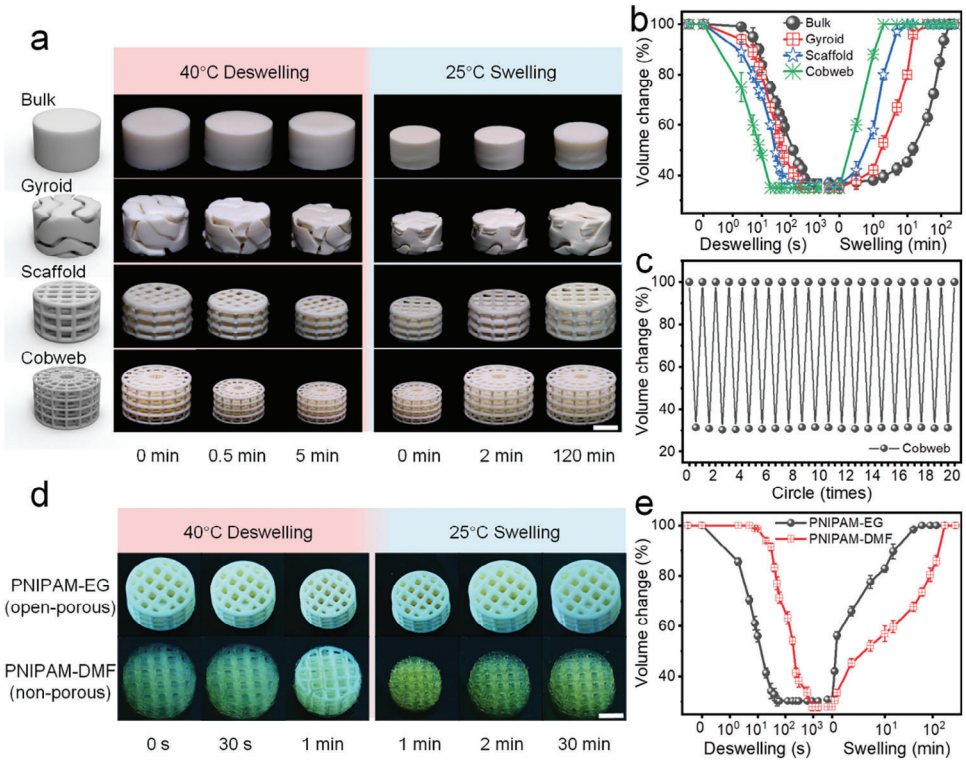

Figure 4. 3D printing of hierarchically porous PNIPAM hydrogels. a) Digital photos and b) deswelling (40 °C) and swelling curves (25 °C) for PNIPAM-EG hydrogels with distinct macroscopic porosity. c) The reversibility of 3D-printed cobweb-shaped cylinder upon 20 cycles of switching temperature between 25 and 40 °C. d,e) Deswelling and swelling behavior of 3D-printed macroscopically porous PNIPAM hydrogel with high and non-porosity. Scale bars in (a) and (d) are 1 cm.

(232 kPa) was higher than that in the direction perpendicular to printing (148 kPa) (Figure S8, Supporting Information). This study highlighted a notable improvement in both mechanical strength and deswelling rate compared with previously reported PNIPAM-based hydrogels (Figure 3g). This enhancement was essential for expanding their practical applications in the fields of soft robotics, solar vapor generation, energy storage, and actuators.[15,22,24,38,40–43]

Following the establishment of a highly porous structure through phase separation to expedite the response rate, we utilized the capabilities of 3D printing to further improve the response speed of the hydrogel structure. We examined printing resolution by creating a series of pillars with different length × width (from 50 μm × 50 μm to 250 μm × 250 μm) and fixed heights (500 μm) (Figure S9, Supporting Information). Subsequently, we applied distinct macro architectures (bulk, gyroid, scaffold, and cobweb) using PNIPAM-EG cylinder hydrogels (**Figure** 4a). Table S2 (Supporting Information) shows the structural information of four cylinders. Among these samples, the cobweb-shaped hydrogel demonstrated the most rapid deswelling and swelling rates, while the bulk hydrogel exhibited the slowest deswelling rate (Figure 4b; Movie S3, Supporting Information). This outcome aligned with the structural, thermo-responsive, and mechanical characterization data shown above, as the cobweb-shaped hydrogel possessed a high porosity that significantly facilitated water diffusion, thereby improving the responsiveness of PNIPAM-EG. Moreover, the cobweb-shaped hydrogel maintained consistent volume changes over 20 cycles of deswelling/swelling, indicating its robustness (Figure 4c). The deswelling/swelling rate of the cobweb-shaped hydrogel composed of PNIPAM-EG was notably faster than that of PNIPAM-DMF (Figure 4d,e), underscoring the unique advantage conferred by the hierarchical porous structure here presented. 3D-printed flower-shaped hydrogels showed the same result (Figure S10, Supporting Information).

3D printing offers precise control over local geometry and dimensions, opening up new possibilities for manipulating the actuation of PNIPAM hydrogels. To showcase this potential, we initially printed six pillars with equal heights (40 mm) but varying diameters (from 5 to 10 mm in 1 mm steps). Reducing the pillar diameter of PNIPAM hydrogels enhanced the deswelling rate and swelling rate of height 43.0% and 32.7 times, respectively, most likely by decreasing the distance for water penetration during swelling and deswelling (**Figure** 5a). Additionally, we fabricated a cage consisting of pillars with the same length but progressively increasing diameter from top to bottom (Figure 5b–d; Movie S4, Supporting Information). The thinner diameter of the upper part of the cage resulted in a faster deswelling rate compared to the lower part. This anisotropic shrinkage led to a change in the pillar angle from 90° to 83°. Once the deswelling of the entire cage reached equilibrium, the pillar angle reverted to 90°. These outcomes highlighted the potential of 3D printing to spatially and temporally control the responsive kinetics of PNIPAM

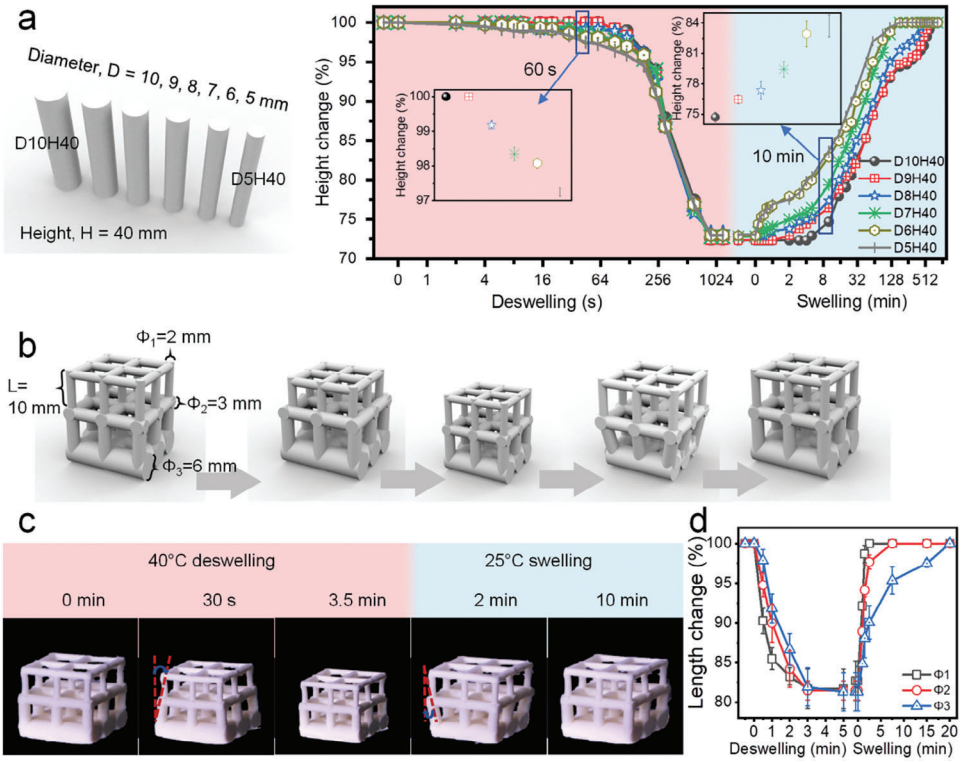

Figure 5. 4D printing of PNIPAM hydrogel cages with programmable actuation. a) Deswelling and swelling behavior of PNIPAM-EG hydrogel pillars with equal height but varying diameter. b) Schematic illustration and c,d) the anisotropic deswelling and swelling behavior of PNIPAM-EG cage made of pillars with the same height but varying diameter.

hydrogels, enabling programmable and complex actuation for advanced applications.

3. Conclusion

We have developed an approach for constructing hierarchically porous PNIPAM hydrogels with rapid responsiveness to temperature stimulus by combining PIPS with 3D printing. We investigated the influence of the porous structure on the responsiveness and mechanical properties of PNIPAM hydrogels and showed that PNIPAM-EG hydrogel exhibited high porosity combined with thin polymer walls due to the phase separation occurring during the polymerization of NIPAM in the presence of EG solvent. Such high porosity and thin polymer structures accelerated water diffusion, as demonstrated by dye diffusion experiments. As a result, high-porosity hydrogels exhibited both faster deswelling and swelling rates and temperature responsiveness when compared to no-porosity or low-porosity hydrogels. Moreover, we successfully fabricated hierarchically porous PNIPAM hydrogels, combining 3D-printed macroporosity with phase-separated sub-micrometer porosity, which exhibited even faster temperature responsiveness of centimeter-scale structures. Furthermore, using 3D printing, we demonstrated the creation of a porous cage capable of programmed responses. Thus, our strategy paves the way for the development of intelligent materials capable of fast, complex, and programmable morphing, which unlocks new possibilities across a range of applications of responsive polymers.

4. Experimental Section

Materials—Ink Preparation: Irgacure 819 was purchased from Ciba. Lithium phenyl-2,4,6-trimethyl benzoyl phosphinate (LAP), methyl orange (MO), ethylene glycol (EG), N-isopropyl acrylamide (NIPAM, 99% pure, stabilized) and N, N'-methylene bisacrylamide (BIS, 99%) were bought from Sigma–Aldrich. N, N-Dimethylformamide (DMF) was purchased from Merck. All chemicals were used as received. Deionized (DI) water was used in the whole experiment.

In brown bottles, 20 wt% NIPAM monomers to solvents, a certain amount of BIS to monomer, solvents, light-absorbing MO dye (0.01% wt total), and 1.5 wt% photoinitiators 819 to NIPAM were mixed. To obtain a clear and homogeneous solution, the inks were sonicated between 0.5 and 2 h, depending on the solvent (DMF and water were sonicated at room temperature for 0.5 and 1 h, respectively; EG was sonicated 2 h at 40 °C). Because photoinitiator 819 was insoluble in water, it was replaced by LAP when the solvent was water.

DLP 3D Printing: For the 3D printing experiments, a commercial desktop DLP printer (Miicraft Prime 110) was employed. The printer was powered by a 385 nm LED projector with a maximum intensity of 1.0 mW cm^{-2} and an XY resolution of 40 µm. The build area was 116 mm × 62 mm × 12 mm, and the layer thickness could be varied between 5 and 500 µm. The ink tank was filled with the prepared ink solution (50 mL). The 3D printing process then began by irradiating the ink for a pre-determined curing time for the layer thickness (50 µm). The 3D-printed objects were carefully detached from the build platform after printing and immersed in water for one week (the water was refreshed every day) to remove the unreacted monomers and porogens and to achieve a fully swollen state.

Transmission: The transmission of 3D-printed PNIPAM hydrogels was measured from a UV–vis spectrometer (Lambda 35, Perkin Elmer) with a 200–800 nm wavelength range. Each hydrogel sample with a size of

2 cm × 5 mm × 50 µm was printed on a glass plate. Three areas of three samples were tested as parallel samples, and every area was scanned 3 times.

Water Content and Solvent Fraction: The water content of 3D-printed PNIPAM hydrogels and the solvent fraction of as-printed PNIPAM gels were measured via gravimetric analysis. Measure the initial weight of the fully hydrated hydrogels/gels (W_{wet}). Placed the hydrogel/gel at 25 °C until a constant weight was achieved, indicating that all water had evaporated. Finally, the weight of the dry hydrogel/gel (W_{dry}) was measured.

$$\text{Water content and solvent fraction} = \frac{W_{wet} - W_{dry}}{W_{wet}} \times 100\% \quad (1)$$

Scanning Electron Microscope (SEM) Measurement: PNIPAM hydrogels were immersed in liquid nitrogen to instantly freeze and then immediately placed in a freeze-drier for 24 h to remove the ice. The freeze-dried hydrogel samples were then coated with ≈, 10 nm thick gold layer using a Cressington Sputter Coater 108. The porous structure of cross-sections of the 3D-printed PNIPAM hydrogels was characterized by a scanning electron microscope (Zeiss LEO 1530) at an operating voltage of 5 kV.

X-Ray Nano-Computed Tomography (Nano-CT): The nano-CT experiments were carried out using the lab-based X-ray microscope Zeiss Xradia 810 Ultra. Freeze-dried EG, water, and DMF PNIPAM samples were prepared by cutting them manually in triangle format to fit within the field of view and glued to the tip of a pin. The samples were scanned over 180° within a field of view of 65 µm, a pixel size of 128 nm, and Zernike phase contrast mode. For each sample, 901 projections were acquired with an exposure time per projection of 25 s (water and DMF) and 30 s (EG). The reconstructions of the projections were carried out using the proprietary software Zeiss Scout and Scan Reconstructor, based on a filtered back projection algorithm. The 2D and 3D visualization and the segmentation of the data were carried out using the Software Dragonfly ORS.[44] The datasets were filtered using a non-local means filter (kernel 3) previously the segmentation. The segmentations were performed using the deep learning algorithm UNet (depth level 5, input dimension 2.5D, initial filter count 64). A cylinder of the segmented data was extracted from the middle of the samples, from which the 3D reconstructed volume was created.

Measurement of Deswelling/Swelling: For Figure 3a,b, 3D-printed PNIPAM cylinders with different porogen (diameter = 10 mm, height = 6 mm) were used. For Figure 4a,b, PNIPAM cylinders with 26 mm diameter and 17 mm height were used. Deswelling curves were obtained by immersing PNIPAM cylinders into a 40 °C water bath and recording the volume change over time by camera. Video screenshots were taken and then the pixel ruler was used to measure length and height. Subsequently, the volume of cylinders was calculated. Swelling curves were obtained using the same technique after immersing the shrunken hydrogels into a 25 °C water bath.

$$\text{Volume change} = \frac{V_t}{V_0} \times 100\% \quad (2)$$

$$\text{Deswelling rate} = \frac{V_0 - V_t}{V_0 \times t} \times 100\% \quad (3)$$

In Figure 3g, normalization was performed according to the responsive rate of the smart hydrogels is inversely proportional to the square of the small dimension of the hydrogel.[45]

$$\text{Normalized deswelling rate} = \frac{V_0 - V_t}{V_0 \times t} \times 100\% \times h^2 \quad (4)$$

V_t is the volume at a certain time t, V_0 is the original volume, and h is the smallest dimension of the sample.

Diffusion Kinetics of RhB Dye: 3D-printed PNIPAM hydrogels (cubes, 5 mm × 5 mm × 5 mm) were immersed into 0.01 wt% RhB dye-water solution at 25 °C for a certain time for absorption until equilibrium was reached. Then, PNIPAM hydrogels with fully swollen RhB dye were soaked in the DI water at 25 °C to release RhB dye for a certain time. The ratios of fluorescent areas were recorded at certain times during absorption and release by using microscopy (Keyence, BZ-X800). RhB fluorescence images were analyzed with ImageJ.

Mechanical Properties: The compressive mechanical properties of PNIPAM hydrogels were measured with a universal testing machine (EZ-LX, Shimadzu) at 25 °C. Each PNIPAM cylinder with a diameter of 10 mm and a height of 6 mm was placed between the self-leveling plates. The compressed rate on the hydrogel sample was 10% min^{-1}. The compressive strain (ϵ) was defined as the ratio of gauge length change (L_0-L) to the initial gauge length of the hydrogel, where L_0 and L were the deformed hydrogel sample's initial gauge length and real-time gauge length, respectively. The compressive stress (σ) is defined as the force applied to the deformed hydrogel sample (F) divided by the deformed hydrogel sample's real-time characteristic cross-sectional area (A). The slope of the stress-strain curve at the corresponding point is used to calculate the hydrogel's Young's modulus (E) at a given compressive strain.

$$E = \frac{\sigma}{\epsilon} \quad (5)$$

Digital Photography: Digital photos were taken using a Canon EOS 80D digital camera.

Statistical Analysis: Unless otherwise stated, all measurements are reported as mean ± standard deviation. One-way and two-way ANOVA with post-hoc tests for multiple comparisons with a significance of 0.05 was performed on individual and grouped data, respectively, using the software GraphPad Prism V8. Statistical significance between treatments is denoted in the figures with (*). *P*-values ⩽ 0.05, 0.01, 0.001, and 0.0001 were labeled as (*), (**), (***), and (****), respectively.

Supporting Information

Supporting Information is available from the Wiley Online Library or from the author.

Acknowledgements

W.L. and Z.W. contributed equally to this work. W.L. thanks the China Scholarship Council (CSC) for a joint Ph.D. scholarship. This work was partly carried out with the support of the Karlsruhe Nano Micro Facility (KNMF, www.knmf.kit.edu), a Helmholtz Research Infrastructure at Karlsruhe Institute of Technology (KIT, www.kit.edu). The Xradia 810 Ultra (nanoCT) core facility was supported (in part) by the 3DMM2O – Cluster of Excellence (EXC-2082/1390761711). R.D. and P.L. acknowledge the support from the Deutsche Forschungsgemeinschaft (DFG, German Research Foundation) via the Excellence Cluster "3D Matter Made to Order" (EXC-2082/1-390761711). This project was partly supported through the Deutsche Forschungsgemeinschaft (DFG) (Heisenbergprofessur project number 406232485, LE 2936/9-1). Z.D. received funding from Natural Science Foundation of Shandong Province (No. 2023HWYQ-051) and Construction Engineering Special Fund of "Taishan Scholars" of Shandong Province (No. tsqn202306371).

Open access funding enabled and organized by Projekt DEAL.

Conflict of Interest

The authors declare no conflict of interest.

Data Availability Statement

The data that support the findings of this study are available from the corresponding author upon reasonable request.

Keywords

4D printing, phase separation, poly(n-isopropylacrylamide), porous structures, responsive speed

Received: March 1, 2024
Revised: June 17, 2024
Published online:

[1] S. Y. Hann, H. Cui, M. Nowicki, L. G. Zhang, *Addit. Manuf.* **2020**, *36*, 101567.
[2] J. T. Miao, M. Ge, S. Peng, J. Zhong, Y. Li, Z. Weng, L. Wu, L. Zheng, *ACS Appl. Mater. Interfaces* **2019**, *11*, 40642.
[3] Z. Wang, Q. Cai, L. Lu, P. A. Levkin, *Small* **2024**, *20*, 2305214.
[4] Y. Wang, H. Cui, T. Esworthy, D. Mei, Y. Wang, L. G. Zhang, *Adv. Mater.* **2022**, *34*, 2109198.
[5] Z. Wang, Y. C. Lai, Y. T. Chiang, J. M. Scheiger, S. Li, Z. Dong, Q. Cai, S. Liu, S. H. Hsu, C. C. Chou, P. A. Levkin, *ACS Appl. Mater. Interfaces* **2022**, *14*, 50152.
[6] A. Halperin, M. Kroger, F. M. Winnik, *Angew Chem Int Ed Engl* **2015**, *54*, 15342.
[7] M. A. Haq, Y. Su, D. Wang, *Mater Sci Eng C Mater Biol Appl* **2017**, *70*, 842.
[8] H. Arslan, A. Nojoomi, J. Jeon, K. Yum, *Adv. Sci. (Weinh)* **2019**, *6*, 1800703.
[9] A. K. Mishra, T. J. Wallin, W. Pan, A. Xu, K. Wang, E. P. Giannelis, B. Mazzolai, R. F. Shepherd, *Sci Robot* **2020**, *5*, 3918.
[10] L. Chen, M. Liu, L. Lin, T. Zhang, J. Ma, Y. Song, L. Jiang, *Soft Matter* **2010**, *6*, 2708.
[11] L. Tang, L. Wang, X. Yang, Y. Feng, Y. Li, W. Feng, *Prog. Mater. Sci.* **2021**, *115*, 100702.
[12] Y. Jian, B. Wu, X. Yang, Y. Peng, D. Zhang, Y. Yang, H. Qiu, H. Lu, J. Zhang, T. Chen, *Supramolecular Mater* **2022**, *1*, 100002.
[13] X. Cui, Z. Liu, B. Zhang, X. Tang, F. Fan, Y. Fu, J. Zhang, T. Wang, F. Meng, *Chem. Eng. J.* **2023**, *467*, 143515.
[14] B. Zhang, X. Gui, P. Song, X. Xu, L. Guo, Y. Han, L. Wang, C. Zhou, Y. Fan, X. Zhang, *ACS Appl. Mater. Interfaces* **2022**, *14*, 8804.
[15] Y. Shi, C. Ma, L. Peng, G. Yu, *Adv. Funct. Mater.* **2015**, *25*, 1219.
[16] K. Depa, A. Strachota, M. Šlouf, J. Brus, *Eur. Polym. J.* **2017**, *88*, 349.
[17] J. Yoon, P. Bian, J. Kim, T. J. McCarthy, R. C. Hayward, *Angew Chem Int Ed Engl* **2012**, *51*, 7146.
[18] S. Wang, W. Y. Wu, J. C. C. Yeo, X. Y. D. Soo, W. Thitsartarn, S. Liu, B. H. Tan, A. Suwardi, Z. Li, Q. Zhu, X. J. Loh, *BMEMat* **2023**, *1*, 12021.
[19] J. Liu, L. Jiang, S. He, J. Zhang, W. Shao, *Chem. Eng. J.* **2022**, *433*, 133496.
[20] R. Yoshida, K. Uchida, Y. Kaneko, K. Sakai, A. Kikuchi, Y. Sakurai, T. Okano, *Nature* **1995**, *374*, 240.
[21] R. Luo, J. Wu, N.-D. Dinh, C.-H. Chen, *Adv. Funct. Mater.* **2015**, *25*, 7272.
[22] J. Liu, W. Xu, Z. Kuang, P. Dong, Y. Yao, H. Wu, A. Liu, F. Ye, *J. Mater. Chem. C* **2020**, *8*, 12092.
[23] Z. Sun, Q. Zhao, S. Ma, J. Wu, *Mater. Horiz.* **2023**, *10*, 179.
[24] Y. Alsaid, S. Wu, D. Wu, Y. Du, L. Shi, R. Khodambashi, R. Rico, M. Hua, Y. Yan, Y. Zhao, D. Aukes, X. He, *Adv. Mater.* **2021**, *33*, 2008235.
[25] Z. Dong, M. Vuckovac, W. Cui, Q. Zhou, R. H. A. Ras, P. A. Levkin, *Adv. Mater.* **2021**, *33*, 2106068.
[26] F. Wang, P. Altschuh, L. Ratke, H. Zhang, M. Selzer, B. Nestler, *Adv. Mater.* **2019**, *31*, 1806733.
[27] Z. Wang, M. Heck, W. Yang, M. Wilhelm, P. A. Levkin, *Adv. Funct. Mater.* **2023**, *34*, 2300947.
[28] K. Hosoya, Y. Kageyama, K. Kimata, T. Araki, N. Tanaka, J. M. J. Fréchet, *J. Polym. Sci., Part A: Polym. Chem.* **1996**, *34*, 2767.
[29] F. Svec, J. M. Frechet, *Science* **1996**, *273*, 205.
[30] S. Eeltink, L. Geiser, F. Svec, J. M. Frechet, *J. Sep. Sci.* **2007**, *30*, 2814.
[31] F. Puza, K. Lienkamp, *Adv. Funct. Mater.* **2022**, *32*, 2205345.
[32] B. Deore, K. L. Sampson, T. Lacelle, N. Kredentser, J. Lefebvre, L. S. Young, J. Hyland, R. E. Amaya, J. Tanha, P. R. L. Malenfant, H. W. de Haan, C. Paquet, *Nat. Commun.* **2021**, *12*, 55.
[33] Z. Dong, H. Cui, H. Zhang, F. Wang, X. Zhan, F. Mayer, B. Nestler, M. Wegener, P. A. Levkin, *Nat. Commun.* **2021**, *12*, 247.
[34] K. Xia, Z. Dong, Q. Sun, R. Debastiani, S. Liu, Q. Jin, Y. Li, U. W. Paetzold, P. Gumbsch, U. Lemmer, Y. M. Eggeler, P. A. Levkin, G. Hernandez-Sosa, *Adv. Mater. Technol.* **2023**, *8*, 2300408.
[35] Y. Yagi, H. Inomata, S. Saito, *Macromolecules* **1992**, *25*, 2997.
[36] J. Burke, The Book and Paper Group Annual.**1984**, *3*.
[37] M. Shibayama, M. Morimoto, S. Nomura, *Macromolecules* **1994**, *27*, 5060.
[38] Y. Li, L. Liu, H. Xu, Z. Cheng, J. Yan, X. M. Xie, *ACS Appl Mater. Interfaces* **2022**, *14*, 32541.
[39] Z. Chen, Y. Chen, C. Chen, X. Zheng, H. Li, H. Liu, *Chem. Eng. J.* **2021**, *424*, 130562.
[40] L. W. Xia, R. Xie, X. J. Ju, W. Wang, Q. Chen, L. Y. Chu, *Nat. Commun.* **2013**, *4*, 2226.
[41] W. J. Zheng, N. An, J. H. Yang, J. Zhou, Y. M. Chen, *ACS Appl. Mater. Interfaces* **2015**, *7*, 1758.
[42] M. Hauck, L. M. Saure, B. Zeller-Plumhoff, S. Kaps, J. Hammel, C. Mohr, L. Rieck, A. S. Nia, X. Feng, N. M. Pugno, R. Adelung, F. Schutt, *Adv. Mater.* **2023**, *35*, 2302816.
[43] Q. Yan, R. Ding, H. Zheng, P. Li, Z. Liu, Z. Chen, J. Xiong, F. Xue, X. Zhao, Q. Peng, X. He, *Adv. Funct. Mater.* **2023**, *33*, 2301982.
[44] http://www.theobjects.com/dragonfly (accessed: February 2022).
[45] Z. Liu, Y. Faraj, X. J. Ju, W. Wang, R. Xie, L. Y. Chu, *J. Polym. Sci., Part B: Polym. Phys.* **2018**, *56*, 1306.